Electronic Supplementary Information

Revealing the effect of LiOH on forming a SEI using a Co magnetic "probe"

*Zhiqiang Zhao[‡a], Wanneng Ye[‡a], Fengling Zhang[‡a], Yuanyuan Pan[a], Zengqing Zhuo[b], Feihu Zou[a], Xixiang Xu[a], Xiancheng Sang[a], Weiqi Song[a], Yue Zhao[a], Hongsen Li[a], Kuikui Wang[a], Chunfu Lin[a], Han Hu[*c], Qinghao Li[*a], Wanli Yang[b], Qiang Li[*a]*

[a]*College of Physics, Weihai Innovation Research Institute, Institute of Materials for Energy and Environment, Qingdao University, Qingdao 266071, China.*
[b]*Advanced Light Source, Lawrence Berkeley National Laboratory, Berkeley, CA 94720, USA.*
[c]*College of Chemical Engineering, China University of Petroleum (East China), Qingdao 266580, China.*

The Supporting information include:

Section S1 Experimental data

Materials synthesis

In a typical procedure, 2.49 g of cobalt acetate tetrahydrate was dissolved in 300 mL of deionized water (DW) to form a homogenous solution. Then, 5 mL of hydrazine hydrate (80 wt%) was added rapidly into the solution and continuously stirred for 24 h at room temperature. The as-formed precursor was washed repeatedly with DW and dried in vacuum at 60℃ for 12 h. Both CoO and CoOOH are prepared from the precursor $Co(OH)_2$. CoO were obtained by annealing the precursor at 450 ℃ in Ar for 2 h. As for CoOOH, 0.20 g of precursor was dispersed in 200 mL DW to form a suspension and adjusted the pH value to about 12 by addition of 1 M NaOH solution. NaClO solution (15.2 wt%, 20 mL) was dropped slowly into the suspension until the color of the suspension turn into brown-black. After full reaction, the as-formed CoOOH was washed repeatedly with DW and dried in vacuum at 60℃ for 12 h.

Material Characterization

X-ray diffraction (XRD) was performed with a Bruker D8 advance diffractometer with Cu Kα radiation. The microstructures were investigated by scanning electron microscopy (SEM, JEOL JSM-7100F) and transmission electron microscopy (TEM, JEOL, JEM-2100F). The valence states were determined with X-ray photoelectron spectroscopy (XPS) on an Axis Ultra DLD spectrometer. After discharging to 0.01V, the battery was disassembled in the glove box, electrolyte on the electrode surface was washed by NMP. During sample transfer, the electrodes were all in Ar atmosphere, and no argon ion etching was carried out before XPS measurement. X-ray absorption spectroscopy (XAS) was performed at Beamline 8.0.1 of the Advanced Light Source (ALS) in Lawrence Berkeley National Lab (LBNL) and Beamline 02B02 at Shanghai Synchrotron Radiation Facility (SSRF). Samples are transferred via specially designed mini-chamber to avoid air exposure. The experiment is conducted at room temperature with energy resolution about 0.15eV. The sXAS spectra were collected using total electron yield (TEY) mode with a probe depth around 10 nm to characterize SEI signal.

Electrochemistry Characterization

The CR2032 coin-type cell were assembled with samples as working electrodes and lithium metal as counter electrodes. Active material, carbon black and CMC were uniformly pasted onto Cu foil in the proportion of 7:2:1 to form the working electrodes. The electrolyte includes 1 m $LiPF_6$ in 1:1:1 w/w/w ethylene carbonate/dimethyl carbonate/ethyl methyl carbonate. Only EC is replaced by fluoroethylene carbonate (FEC) in the adjusted electrolyte, other conditions remain unchanged. Usually, the electrochemical performance was tested on a Neware Battery

Tester system (CT- 3008W) at 100 mA g^{-1} current density within a voltage window of 0.01−3 V.

Magnetic Characterization

The nonmagnetic flexible packaging cells were assembled using the same counter electrode and electrolyte as the coin batteries. Magnetic measurements were performed on a physical property measurement system (PPMS, Quantum Design) with the temperature of 300 K. Cyclic voltammetry (CV) measurement and magnetic measurement were carried out on the battery at the same time to ensure that the magnetic signal reflected the electrochemical process in real time.

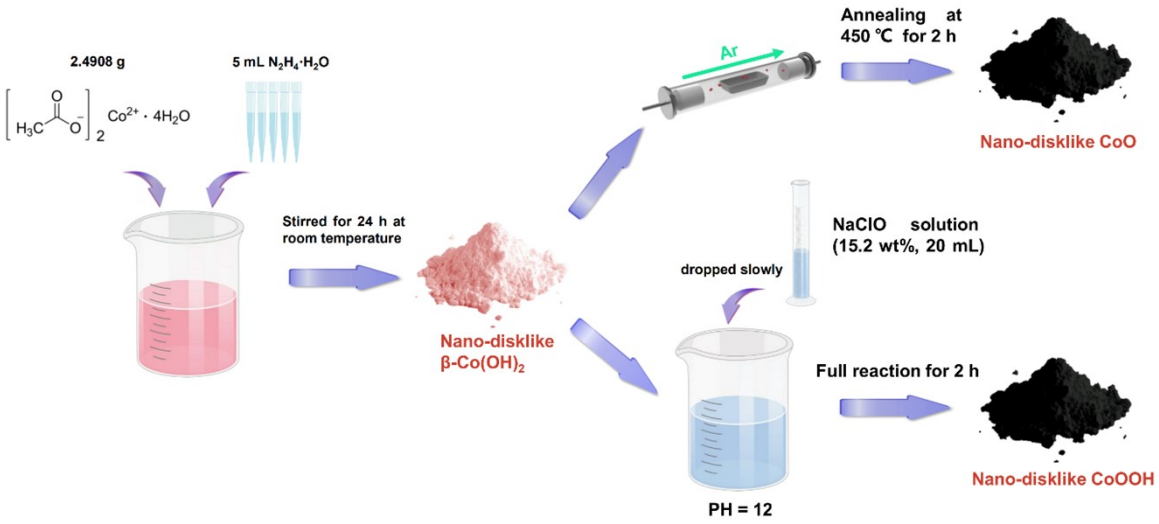

Section S2. Supplementary Figures

Figure S1. Schematic of products synthesis.

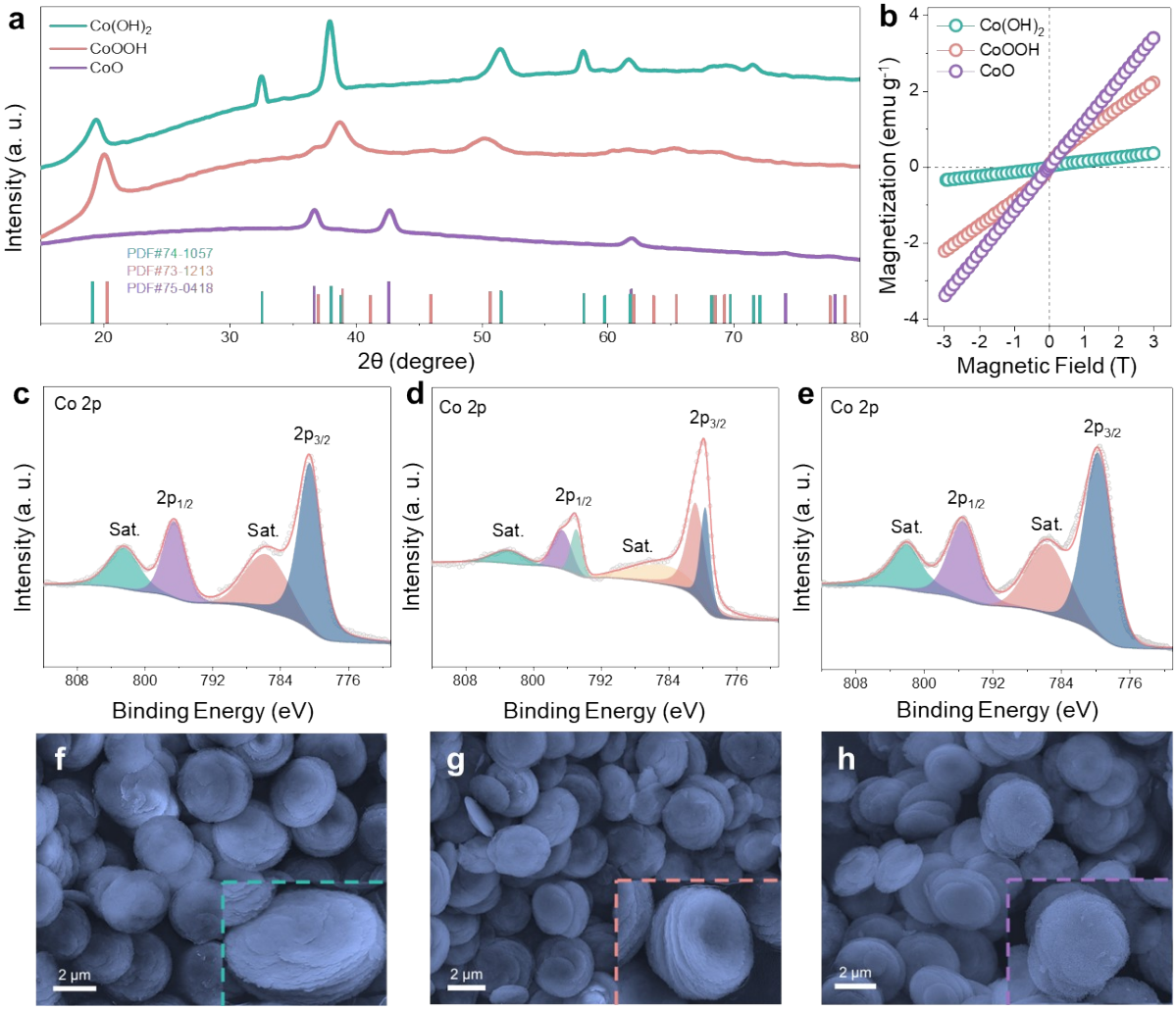

Figure S2. Characterizations of initial materials. (a) XRD patterns of $Co(OH)_2$, CoOOH and CoO (b) magnetic hysteresis (MH) curves of three materials XPS high-resolution Co 2p spectrum for (c) $Co(OH)_2$, (d) CoOOH and (e) CoO. FESEM images of (f) $Co(OH)_2$, (g) CoOOH and (h) CoO.

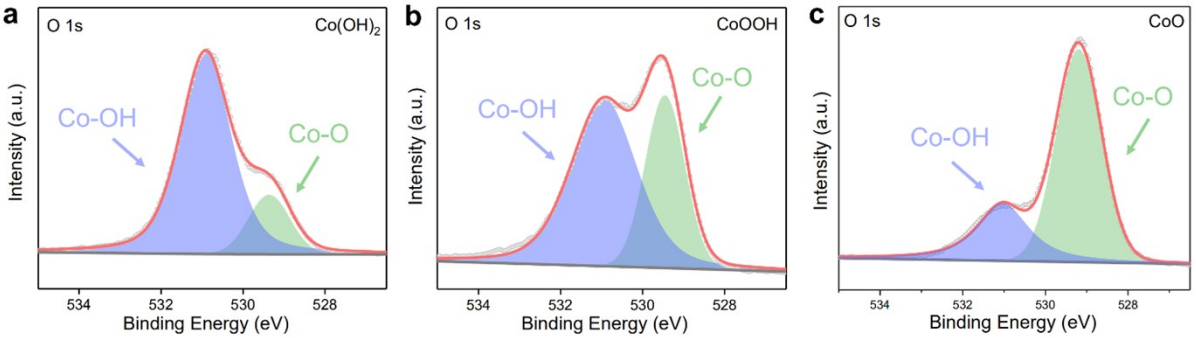

Figure S3. XPS high-resolution O 1s spectrum for (a) $Co(OH)_2$ (b) CoOOH and (c) CoO. Two peaks located at about 530.3 and 529.1 eV are corresponding to Co-OH and Co-O bonds, respectively, the ratio of two peaks shows the change of the materials from $Co(OH)_2$ to CoOOH and then to CoO.

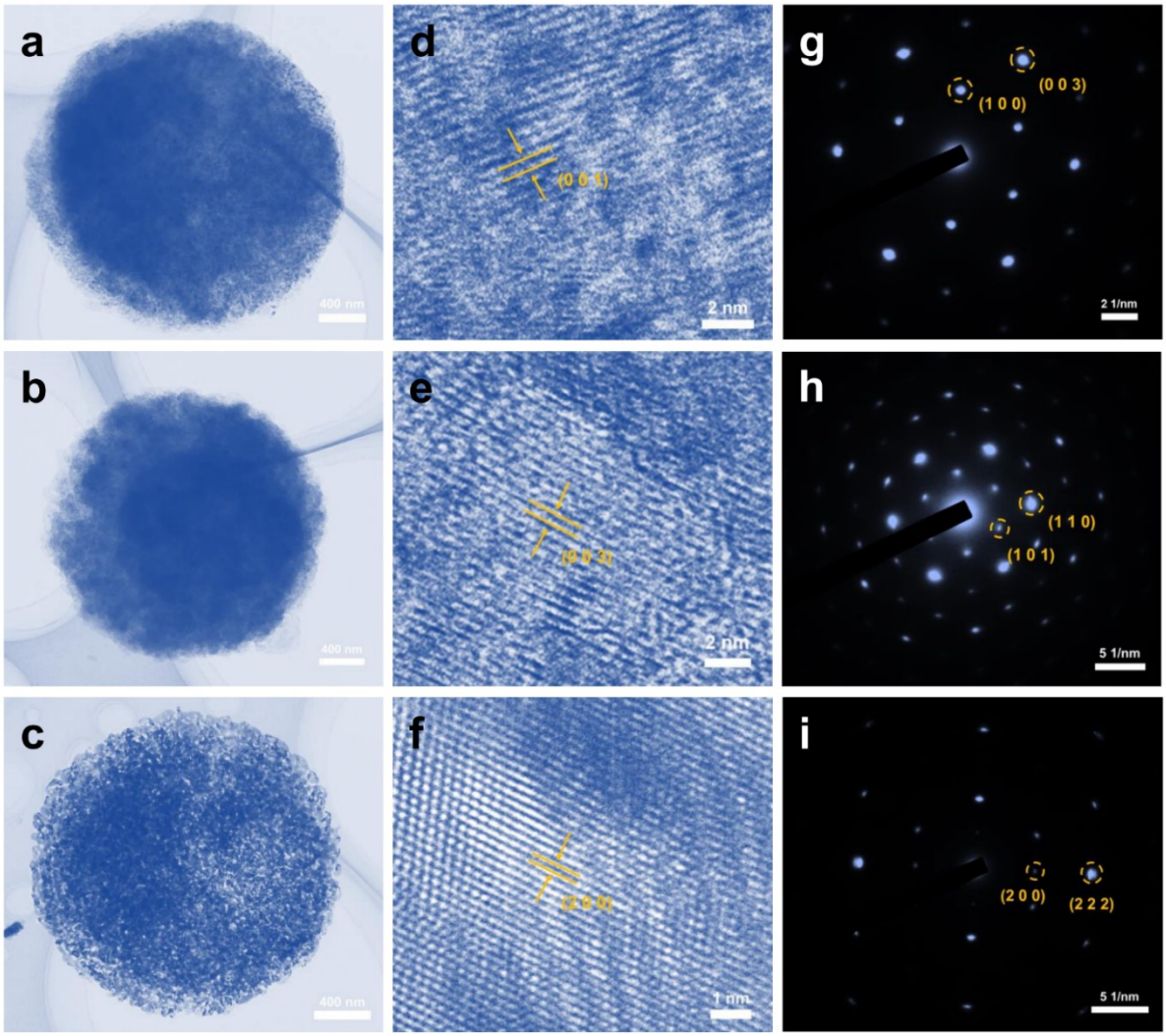

Figure S4. TEM images of three materials. TEM images of the prepared nano-disklike (a) $Co(OH)_2$ (b) CoOOH and (c) CoO, HRTEM images of (d) $Co(OH)_2$ (e) CoOOH and (f) CoO, accompanied by selected area electron diffraction (SAED) of (g) $Co(OH)_2$ (h) CoOOH and (i) CoO.

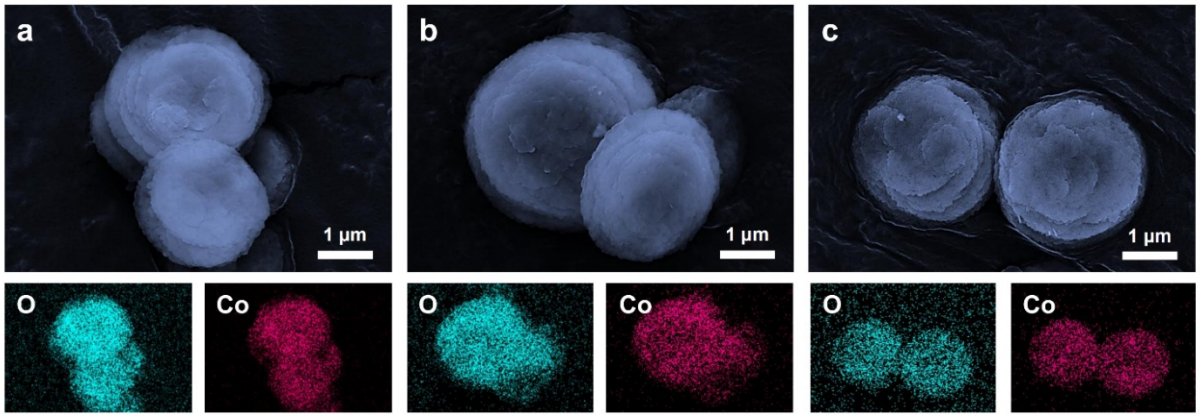

Figure S5. Energy dispersive X-ray spectroscopy (EDS) elemental maps using SEM. (a) $Co(OH)_2$ (b) CoOOH and (c) CoO.

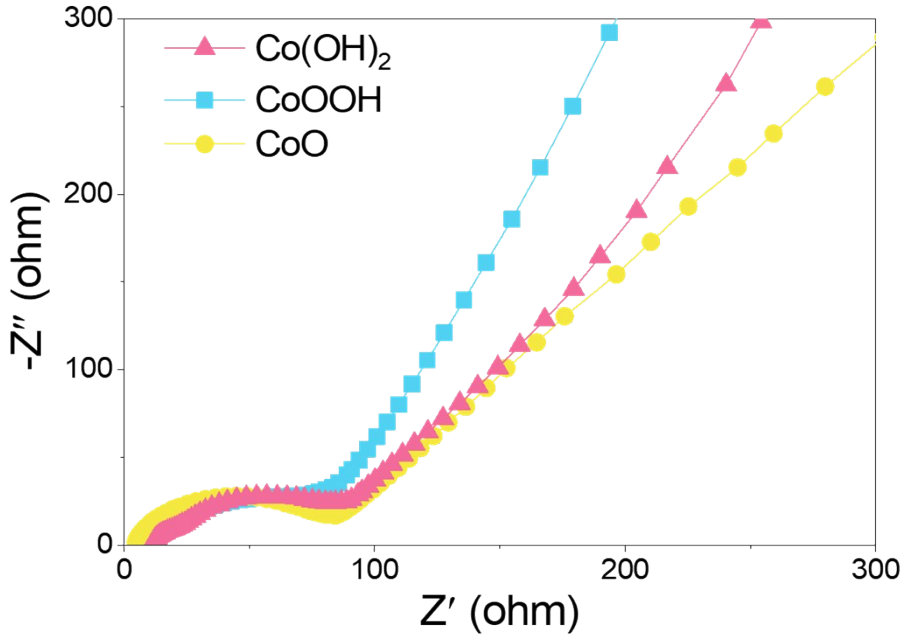

Figure S6. Nyquist curves of three initial materials.

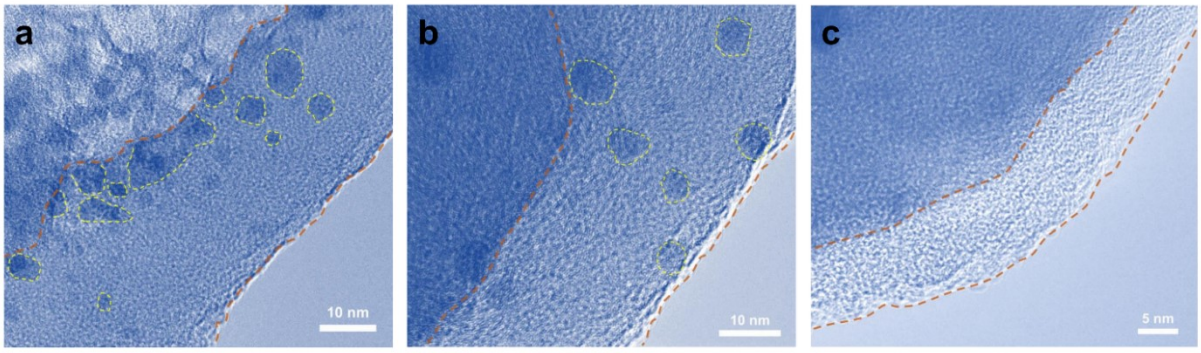

Figure S7. HRTEM images of electrode (discharged to 0.01 V). (a) $Co(OH)_2$ (b) CoOOH and (c) CoO. SEI boundaries are marked with red dotted lines, and dissolved inorganic particles are marked with yellow dotted lines.

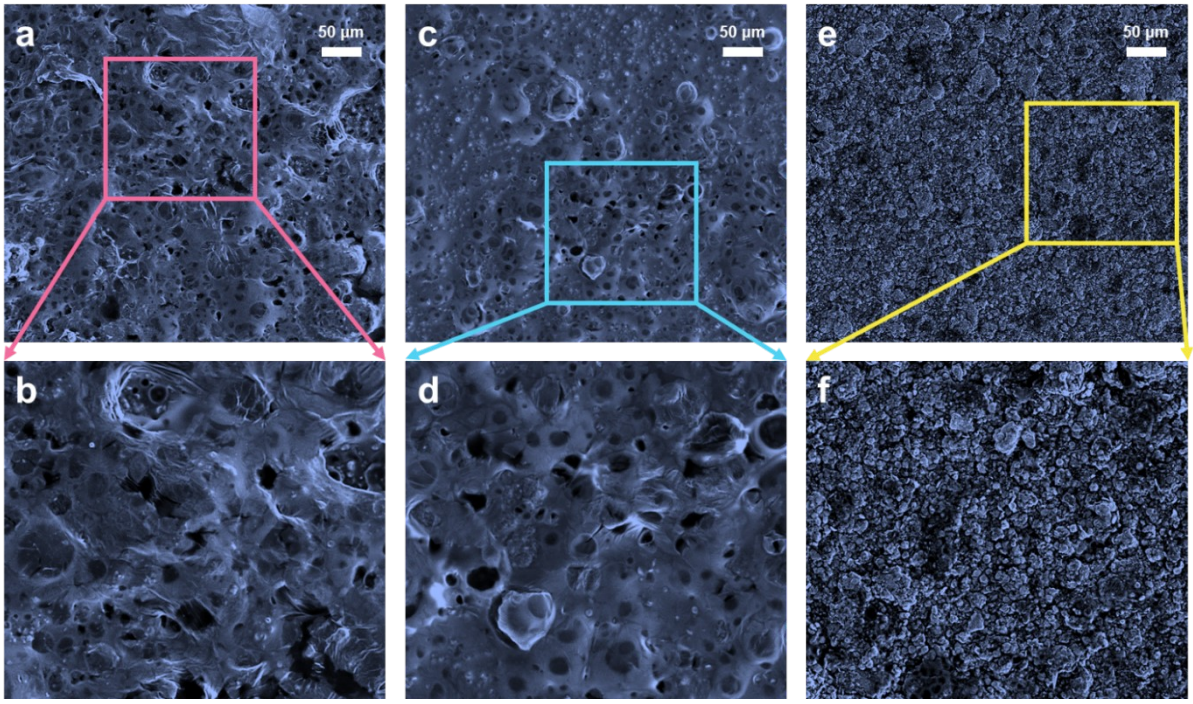

Figure S8. Surface morphology of three materials. (a), (b) $Co(OH)_2$ (c), (d) CoOOH and (e), (f) CoO.

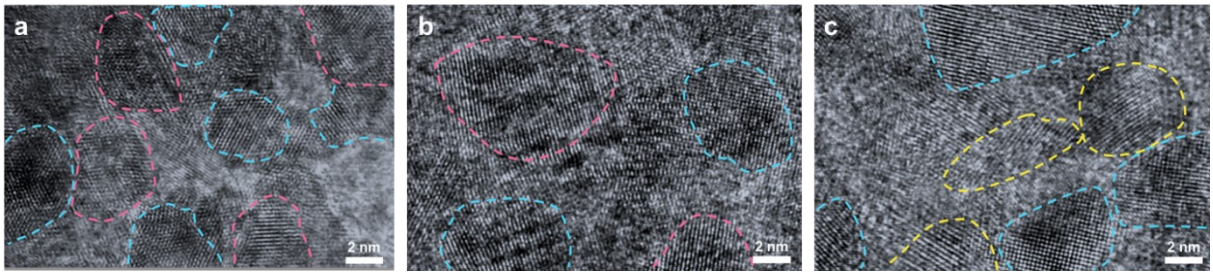

Figure S9. Particle distribution of reduction products of three materials. Blue, red, and yellow lines represent Co, LiOH, and Li_2O, respectively. (a) Co(OH)2, (b) CoOOH, and (c) CoO.

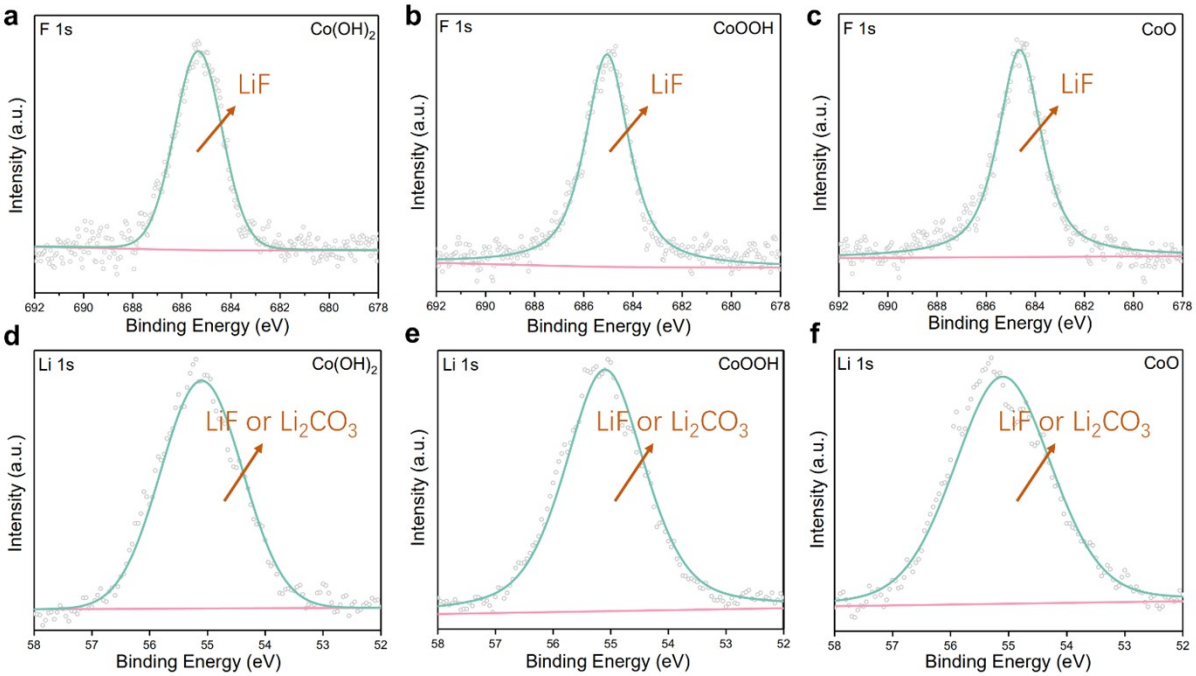

Figure S10. XPS measurements of electrode (discharged to 0.01 V). XPS high-resolution F 1s spectrum for (a) $Co(OH)_2$, (b) CoOOH and (c) CoO. And XPS high-resolution Li 1s spectrum for (d) $Co(OH)_2$, (e) CoOOH and (f) CoO.

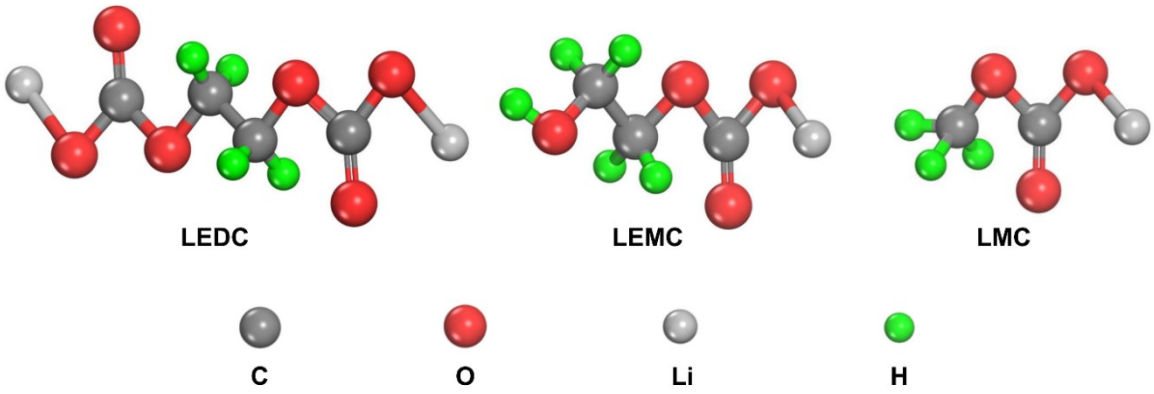

Figure S11. Structure diagram of LEDC, LEMC and LMC.

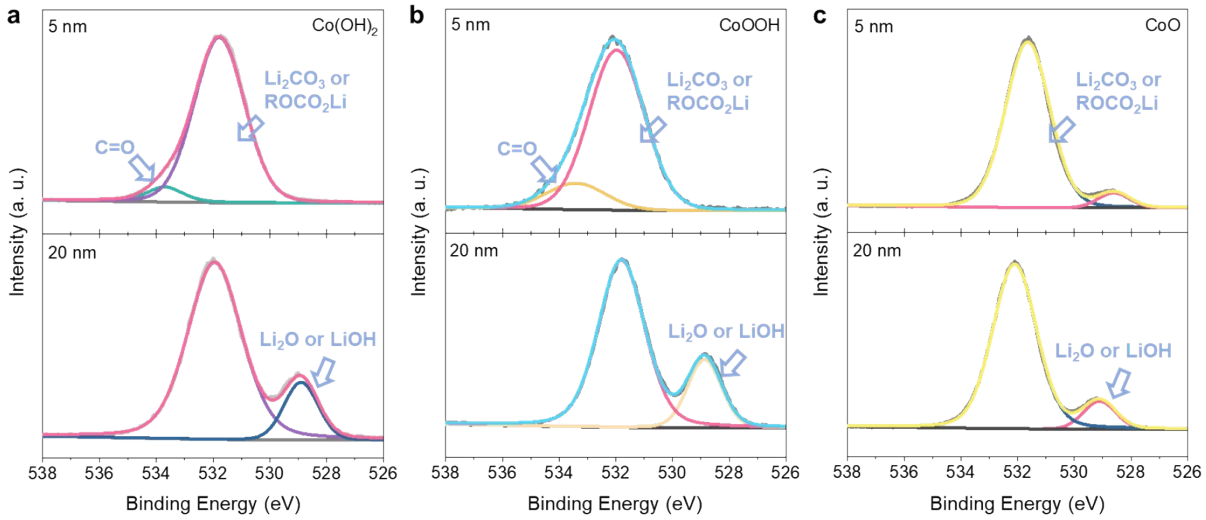

Figure S12. O 1s spectrum XPS measurements of three materials (discharged to 0.01 V) at different etching depths (5 nm and 20 nm). (a) $Co(OH)_2$, (b) CoOOH, and (c) CoO.

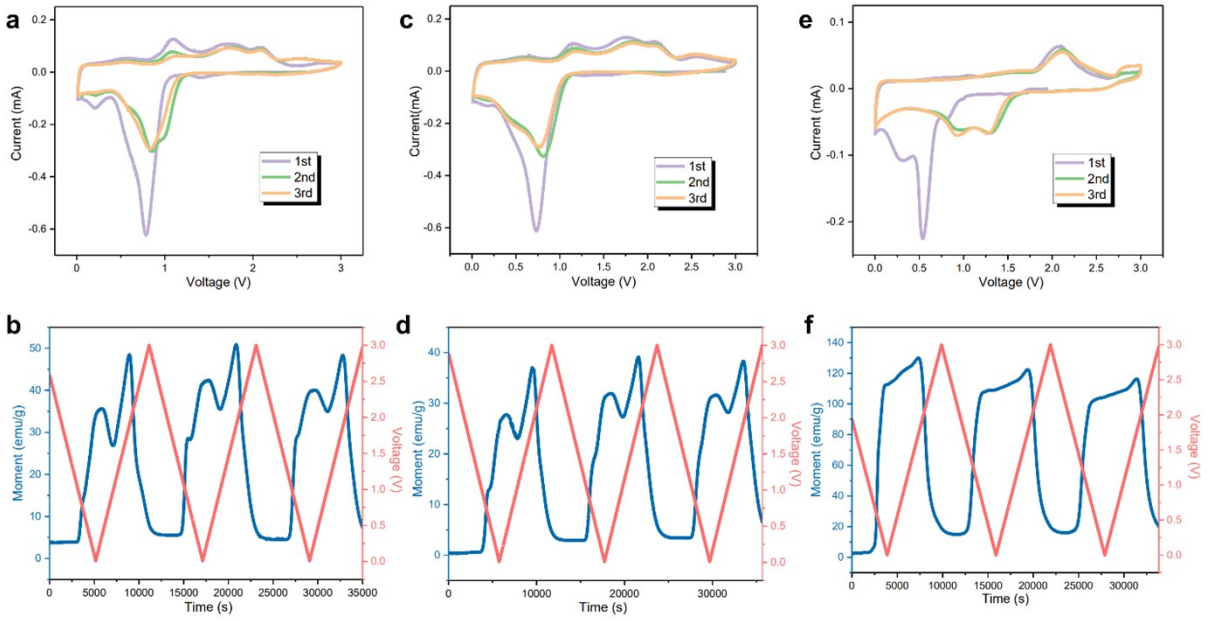

Figure S13. CV curves of three materials electrodes and corresponding magnetic response profiles. (a) CV curve and (b) magnetic response profile of $Co(OH)_2$ electrode; (c) CV curve and (d) magnetic response profile of CoOOH electrode; (e) CV curve and (f) magnetic response profile of CoO electrode. All the CV measurements were performed at a scan rate of 0.5 mV s^{-1} with a potential window of 0.01-3 V, *operando* magnetometry were performed in an applied magnetic field of 3 T.

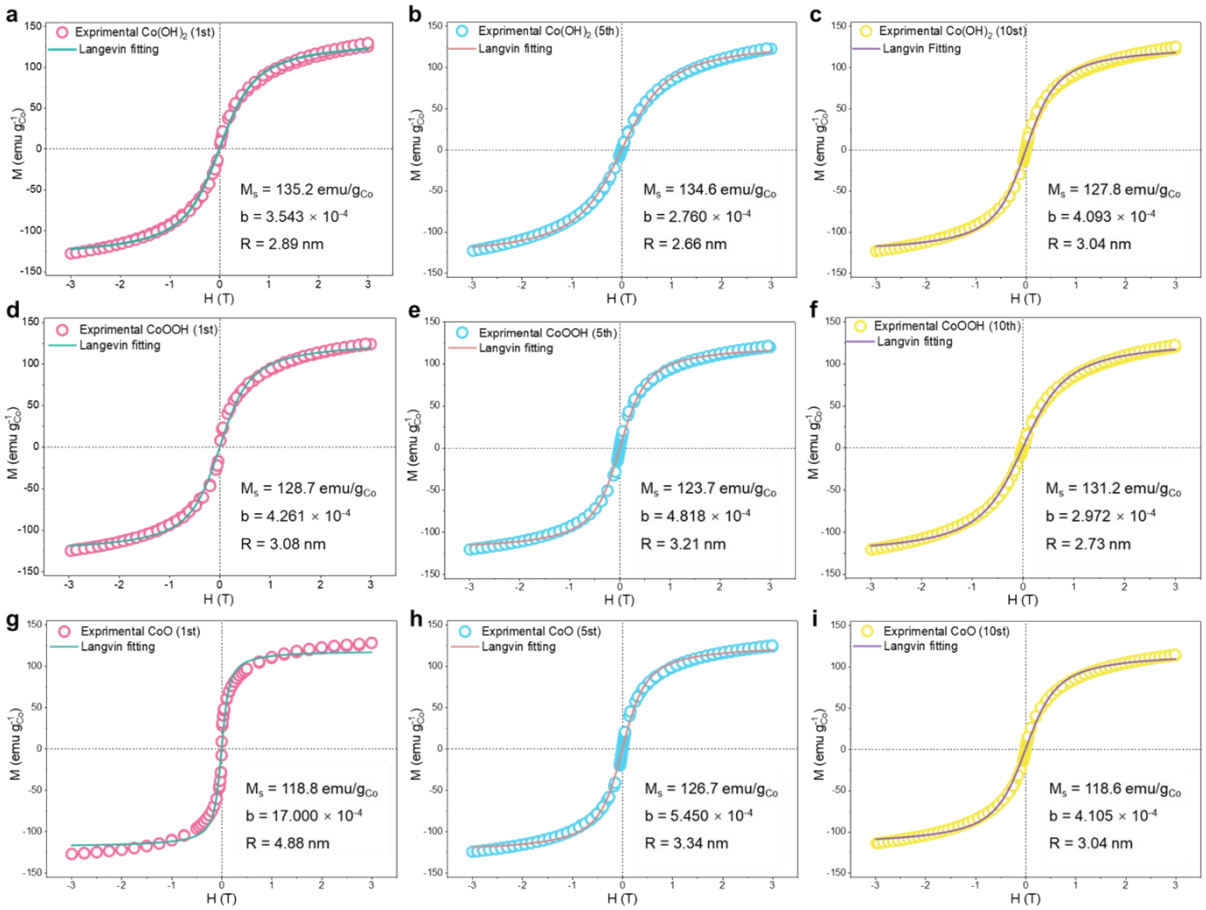

Figure S14. Ex-situ M-H measurement and Langevin fit for three materials with different cycles.

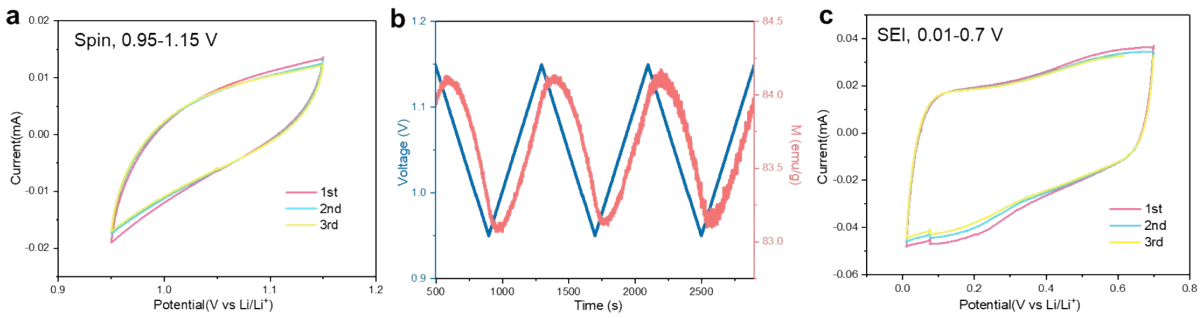

Figure S15. CV curves of $Co(OH)_2$ electrodes and corresponding magnetic response profiles. (a) CV curve with a potential window of 0.95-1.15 V and (b) corresponding magnetic responses profiles. (c) CV curve with a potential window of 0.01-0.7 V. All the CV measurements were performed at a scan rate of 0.5 mV s^{-1}, *operando* magnetometry were performed in an applied magnetic field of 3 T.

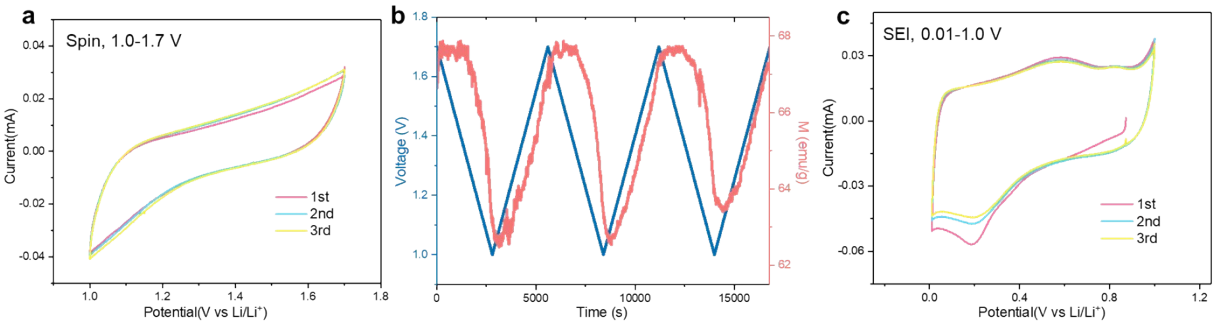

Figure S16. CV curves of CoOOH electrodes and corresponding magnetic response profiles. (a) CV curve with a potential window of 1.0-1.7 V and (b) corresponding magnetic responses profiles. (c) CV curve with a potential window of 0.01-1.0 V. All the CV measurements were performed at a scan rate of 0.5 mV s^{-1}, *operando* magnetometry were performed in an applied magnetic field of 3 T.

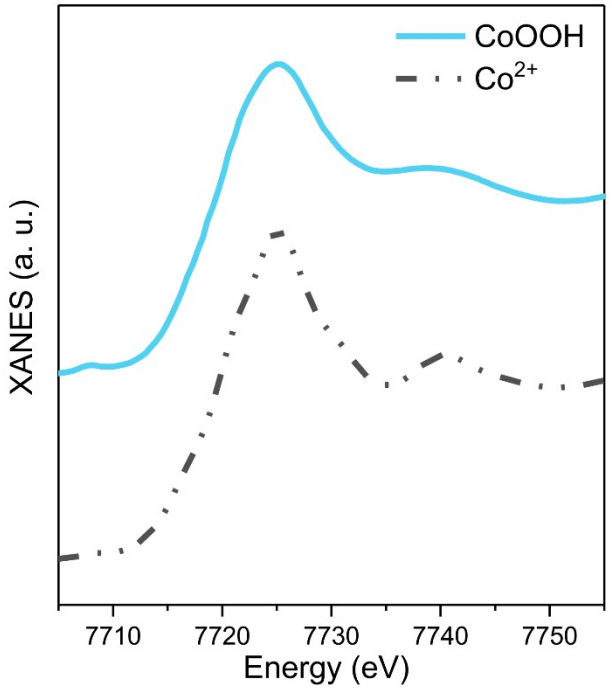

Figure S17. Co K-edge XAS spectra of CoOOH (fully charged to 3 V).

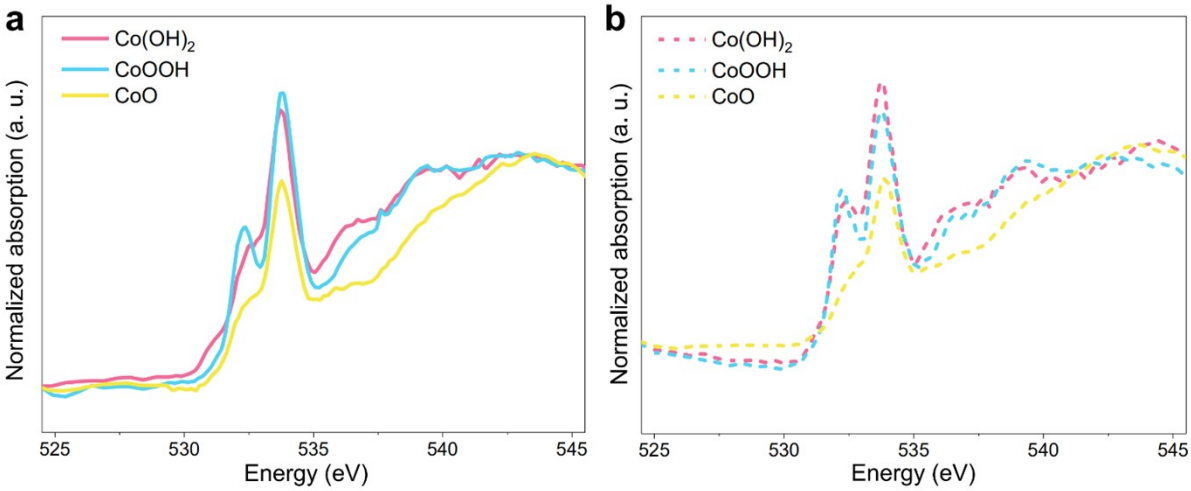

Figure S18. Intensity contrast of Li_2CO_3 peak among $Co(OH)_2$ CoOOH and CoO. (a) discharged to 0.01 V, (b) charged back to 1.7 V.

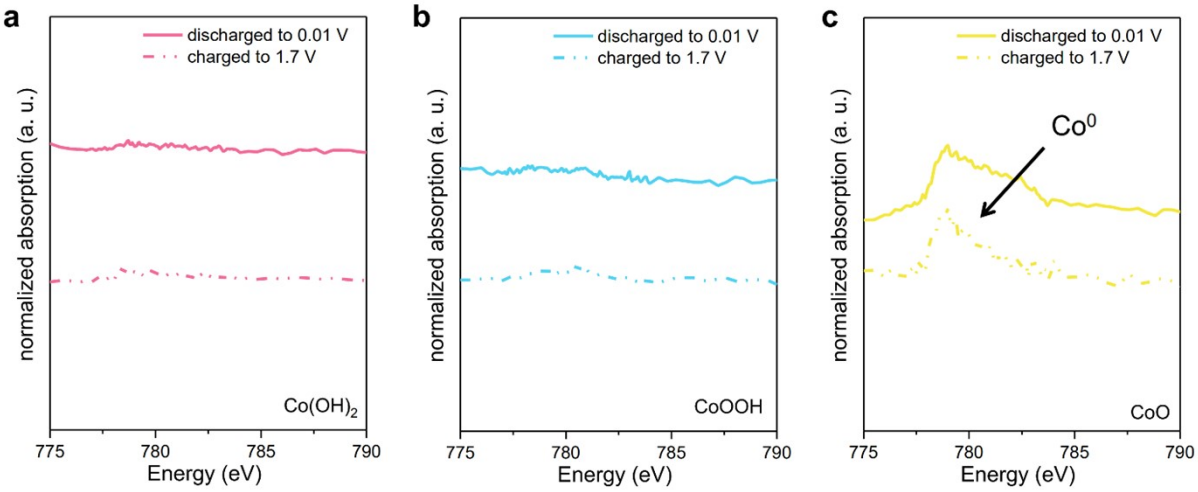

Figure S19. Co L-edge soft XAS spectra (TEY model) of three materials. (a) $Co(OH)_2$ (b) CoOOH and (c) CoO.

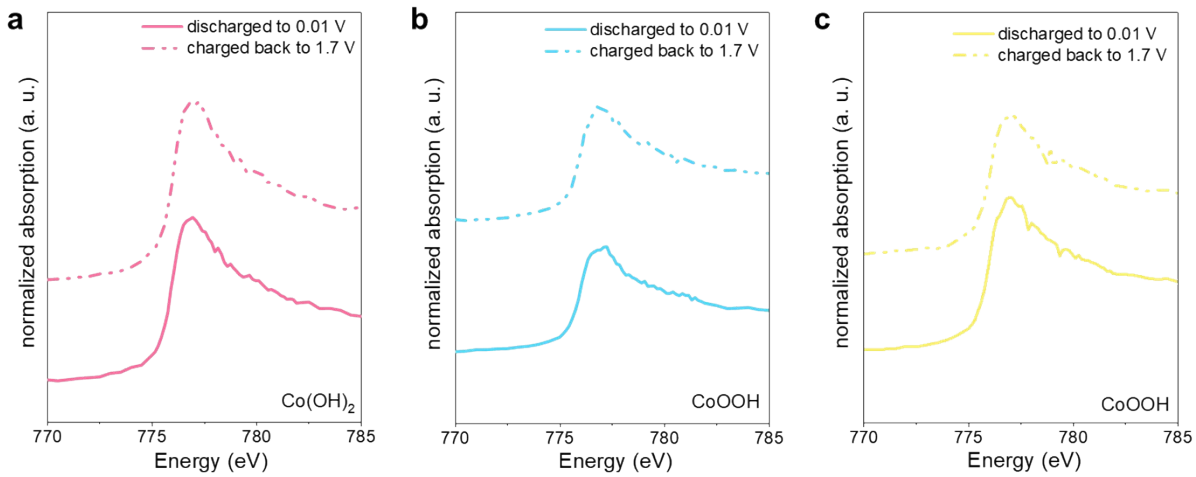

Figure S20. Co L-edge soft XAS spectra (TFY model) of three materials. (a) $Co(OH)_2$ (b) CoOOH and (c) CoO.

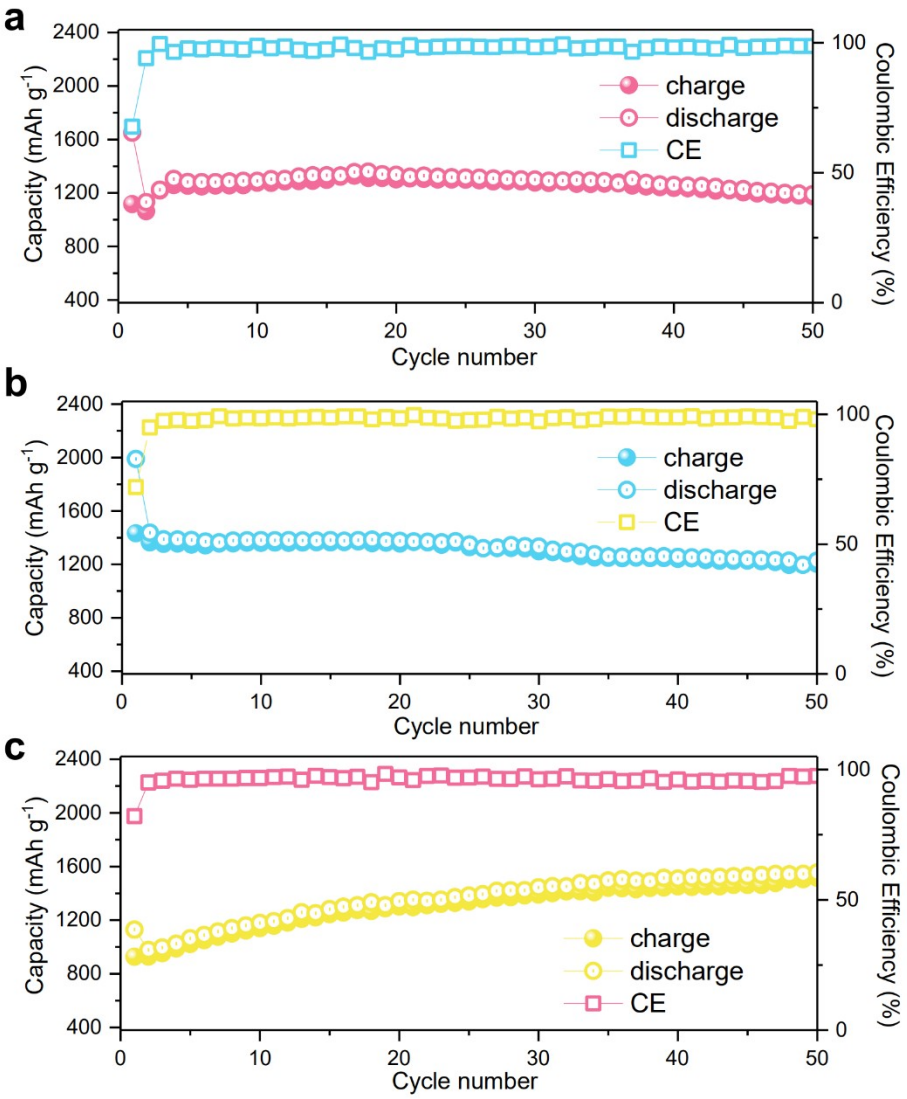

Figure S21. Cycle performance of three materials at a current density of 100 mA g^{-1} using adjusted electrolyte. (a) $Co(OH)_2$ (b) CoOOH (c) CoO.

Section S3. Supplementary tables

Table S1. Capacity decline of transition metal hydroxide electrode materials during initial cycles in different works. Since the exact capacity is not given in the paper, the remaining capacity was estimated from the figures.

Products	Initial capacity/second cycle capacity	Discharge current	Cycle number	Remaining capacity
$Co_2(OH)_2CO_3$	1900/1550 mAh g^{-1}	100 mA g^{-1}	10	1200 mAh g^{-1}
Ni-Fe-OH	1850/1100 mAh g^{-1}	1/2 C	10	600 mAh g^{-1}
$Co(OH)_2$	1550/850 mAh g^{-1}	1 C	10	550 mAh g^{-1}
$Co(OH)_2$ film	2000/1900 mAh g^{-1}	400 μA/cm^2	10	1600 mAh g^{-1}

Section S4. Magnetic background treatment (before cycle) and proof for magnetic signal source (during cycle)

Magnetic background treatment: Before operando magnetometry, magnetization of electrode material will be tested. After assembling the electrode materials into operando battery, overall magnetization of operando battery will be tested too. The excess magnetization of operando battery compared with the electrode material is the magnetic background. Since all components in initial battery are paramagnetic, magnetic background can be directly subtracted. The in-situ magnetic signal without magnetic background (caused by battery structure) can be obtained through this method.

Proof for magnetic signal source: In order to further eliminate magnetic noise that may be introduced during cycle, operando magnetometry were performed on carbon-only electrode material. As shown in Figure S22, magnetic signal changes very little during cycle process, which is negligible compared with the magnetic signal brought by Co^0 nanoparticles. Therefore, magnetic signal that has minus magnetic background can be completely attributed to Co, while other possible factors can be ignored.

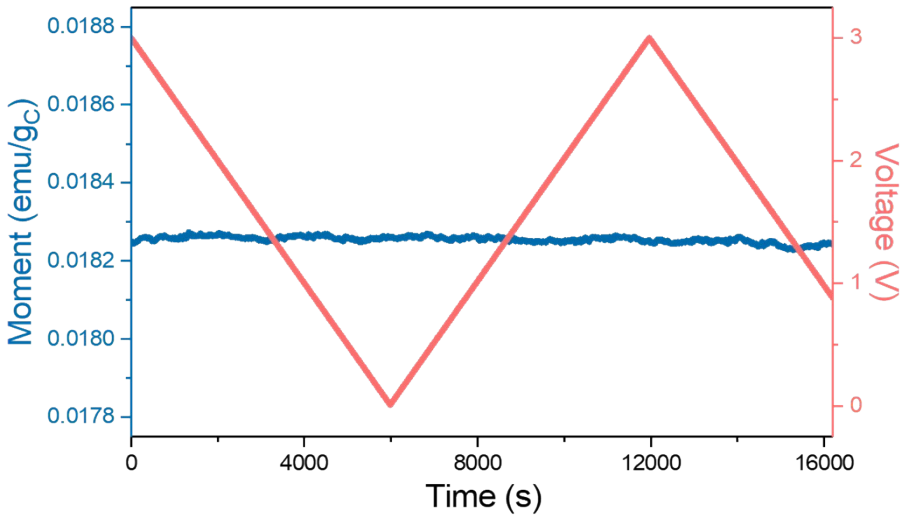

Figure S22. Operando magnetic signal of carbon electrode.

Section S5. Langevin fitting of magnetic hysteresis curves.

Fitting of magnetic hysteresis curves followed Tamion[1]. Some parameters determined from the fits were: the standard deviation of the iron particle size in a normal distribution σ, the paramagnetic signal contribution to the hysteresis curve χ, the number of iron particles N per total sample mass, and the mean diameter of the particles in a normal distribution $\bar{D}$[8].

The magnetic moment of superparamagnetic iron grains with diameters following an iron particle size distribution function (PDF) in a magnetic hysteresis curve can be described by:

$$M(H,T) = N\int_0^{\infty} \frac{M_s \pi D^3}{\sigma}\left[\coth(x) - \frac{1}{x}\right] PDF(D)dD + \chi H \tag{1}$$

Where M_S is the saturation magnetization (Co: 162 emu g^{-1}) and D is the iron particle diameter. The argument χ can be written as:

$$\chi = \frac{\mu_0 M_s \pi D^3 H}{6K_b T} \tag{2}$$

Where K_b and μ_0 is the usual physical constants, and H is the magnetic field. The iron particle distribution function was deemed to be a normal distribution:

$$PDF(D) = \frac{1}{\sqrt{2\pi\sigma^2}} exp\left(-\frac{(D-\bar{D})^2}{2\sigma^2}\right) \tag{3}$$

Finally, we set μ_p to the magnetic moment per particle, and make μ_p/K_bT equal to b. Then, in combination with formulas (1) (2) (3), the following simplified form is obtained:

$$M = M_s \cdot \left(\coth(b \cdot H) - \frac{1}{b \cdot H}\right) \tag{4}$$

According to formula (4), we obtained the Langevin fitting curves of Figure 4d~f and further calculated that the saturation magnetization values M_S of $Co(OH)_2$ CoOOH and CoO were 135.2, 128.7 and 118.75 $^{emu\ g_{Co}^{-1}}$, and b were 3.543×10^{-4} 4.261×10^{-4} and 0.0017 emu erg^{-1}, respectively. Note that the fitting curve could not completely coincide because of the uneven size of Co particles produced by lithiation, so that the value of M_S was slightly lower than the actual value[1].

Section S6. Detailed explanation of *operando* magnetometry results.

In 3*d* transition metals (Co), the different filling of spin-up and spin-down *d* bands is responsible for the ferromagnetism (Figure S23a). The spin-up *d* bands are filled much more than the spin-down *d* bands. The net magnetization is given by $M = (N_{\uparrow} - N_{\downarrow})\mu_B$, where $N_{\uparrow}$ and $N_{\downarrow}$ are the total number of electrons for each spin and μ_B is the Bohr magneton. During discharging to low voltage range, a space charge region will be established, where electrons accumulate at the surface of Co nanoparticles[2]. At this point, the electrons will converge in the 3*d* orbit of Co nanoparticles[3]. The electrons accumulate more in the spin-minority bands than in the spin-majority bands because of Co spin splitting band (Figure S23b), result in magnetization decrease. In the subsequent process, due to the involvement of Co promoting SEI formation[4, 5], the electrons filling in 3*d* orbit will be affected (red two-way arrow in Figure S23b), lead to magnetization change[6]. Thus the magnetization variation of $Co(OH)_2$ and CoOOH between V_2 and V_4 can be attributed to more intense SEI reaction.

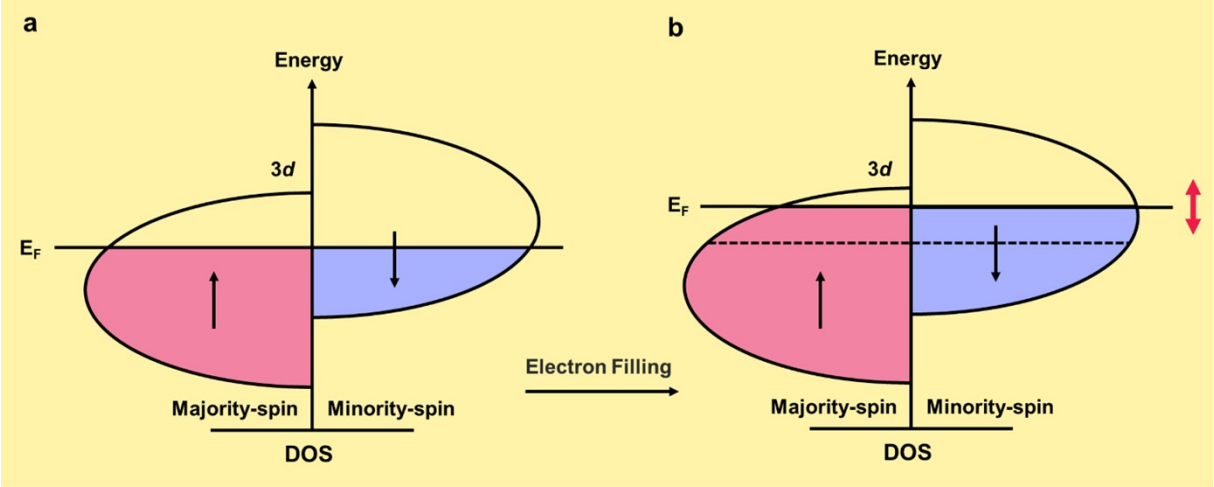

Figure S23. Spin-polarized electron density of states (DOS) schematic. (a) original spin-polarized DOS and (b) spin-polarized DOS after electron filling.

Section S7. Theoretical calculation details.

The first-principle calculations are based on the projector augmented wave (PAW) method implemented in the Vienna ab initio simulation package (VASP) including spin-orbit interactions[7, 8]. The exchange correlation potential is treated in the generalized gradient approximation (GGA) with the Perdew-Burke-Ernzerhof (PBE) forms[9]. We used a cut-off energy of 500 eV as the plane-wave basis set. The geometry optimization is curried out until the maximum energy during geometry optimization is converged to within 1×10^{-6} eV. A vacuum buffer space of at least 12 Å is set.

Section S7.1. Calculation details of the adsorption of H ions on Co surface and CoH_x formation.

In order to study the effect of H atom adsorption on Co magnetization, five layers of 3 × 3 supercells of Co (0 0 0 1) surfaces are built, and H atoms are adsorbed on one side of Co (0 0 0 1) surfaces as shown in Figure S24. Bulk Co^0, $CoH_{1/3}$, CoH, and CoH_3 were built to study the magnetic changes caused by CoH_x compounds, in which Co and H are bonded, as shown in Figure S25. A vacuum buffer space of at least 12 Å is set for the interface calculation. We used 4 × 4 × 1 Monkhorst-Pack grid for *k*-point sampling in the geometry optimization calculations.[10]. For Co^0, $CoH_{1/3}$, CoH, and CoH_3, *k* points were sampled by 8 × 8 × 8, 11 × 11 × 2, 7 × 7 × 7 and 10 × 10 × 10 Monkhorst-pack grids, respectively.

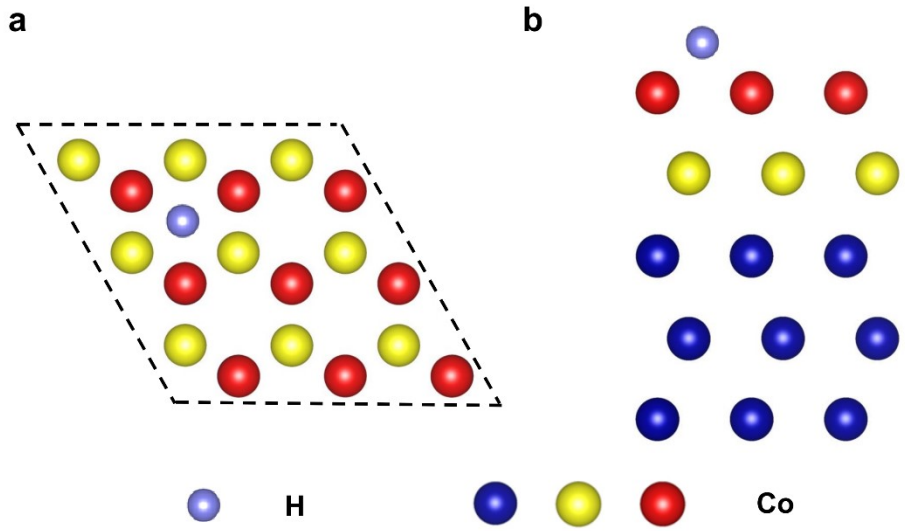

Figure S24. The atomic structure of the adsorption of H ions on Co (0 0 0 1) surface. (a) Top and (b) side view of the adsorption of H ions on Co (0001) surface. The red balls represent the outermost Co, the yellow ones the Co in secondary layer and the blue ones the internal Co.

Table S2. Spin magnetic moment of Co varies with the number of H adsorbed.

Number of H adsorbed	0	1	2	3	4
Spin Mag (μ_B per Co atom)	1.781	1.767	1.756	1.749	1.736

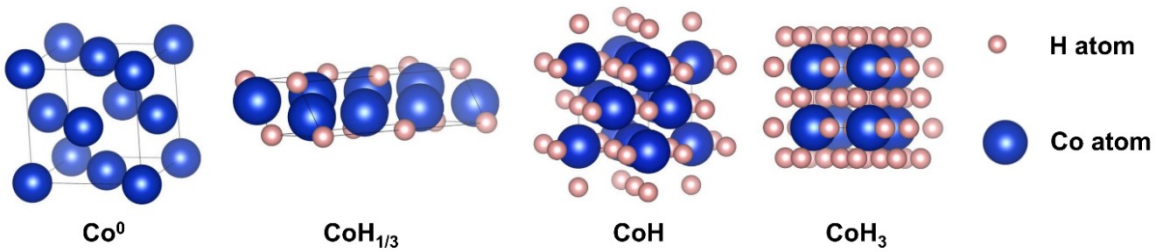

Figure S25. Model diagram of bulk Co^0, $CoH_{1/3}$, CoH, and CoH_3 (from left to right).

Table S3. Spin magnetic moment of Co varies with the number of x in CoH_x.

Materials types	Co^0	$CoH_{1/3}$	CoH	CoH_3
Spin Mag (μ_B per Co atom)	1.767	1.596	1.509	0.156

Based on the above calculation results, magnetic moment change of Co with the influence of H (Co adsorption H and CoH_x formation) are shown in Figure S26. It is demonstrated that the magnetic moments indeed change no matter after absorption of H on Co surface or the formation of CoH_x. Moreover, in both cases, the magnetic moments of Co decrease gradually with the increase of H number. This indicates that the overall lower magnetization of $Co(OH)_2$ and CoOOH in *operando* environment is related to the influence of H atom.

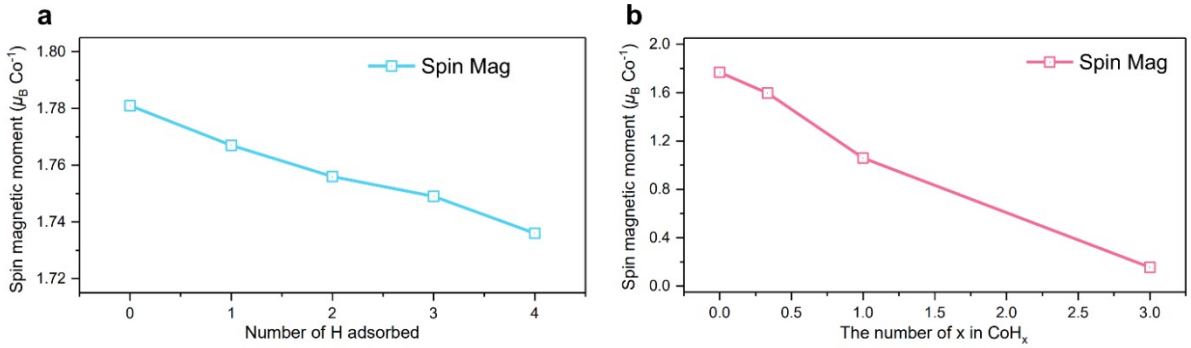

Figure S26. Spin magnetic moment of Co varies with the number of H. (a) H adsorbed and (b) x in CoH_x.

Section S6.7. Calculation details of the transition from LEDC to LEMC

Four molecular models of LEDC, LEMC, Li_2CO_3 and LiOH were constructed. The 3 × 3 supercells of three layers of Co (0 0 0 1) surface were constructed, and LEDC, LEMC, Li_2CO_3 and LiOH molecules were adsorbed on the side of Co (0 0 0 1) surface. Specific structure is shown in Figure 27. Based on these structural designs, we calculated Gibbs free energy of the

reaction from LEDC to LEMC. The reaction carried out on Co surface is to verify catalytic effect of Co. For geometric optimization calculation, we used 3 ×3 ×3 and 2 × 2 × 1 Monkhorst-Pack grids to perform K-point sampling on four molecular models and adsorption models, respectively[10]. Vaspkit was used to calculate the thermal energy correction of the Gibbs free energy at room temperature (298.15 K)[11]. The Gibbs free energy is defined as: $G = H - TS = E_{DFT} + ZPE + E_H - T*S$, where H, T, S, EDFT, ZPE and EH are the enthalpy, temperature, entropy, total energy after atomic relaxation by DFT, zero-point energy and enthalpy contribution of each system, respectively.

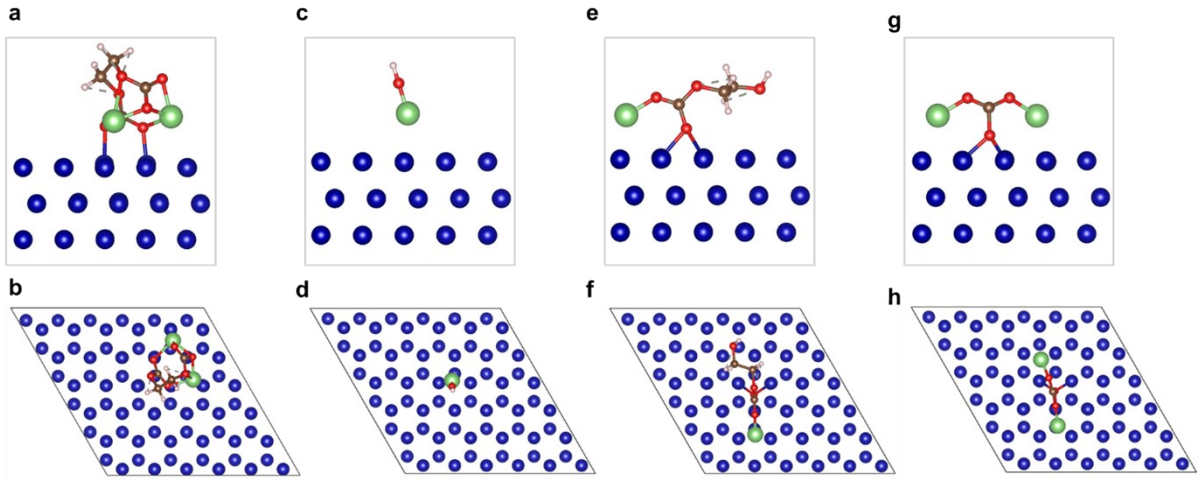

Figure S27. The atomic structure of LEDC LiOH LEMC and Li_2CO_3 and their top/side view adsorbed on Co surface. (a) side and (b) top views of LEDC on the Co surface; (c) side and (d) top views of LiOH on the Co surface; (e) side and (f) top views of LEMC on the Co surface; (g) side and (h) top views of Li_2CO_3 on the Co surface.

References

1. M. Gossler, M. Albu, G. Klinser, E. M. Steyskal, H. Krenn and R. Wurschum, Magneto-Ionic Switching of Superparamagnetism, *Small*, 2019, **15**, 1904523.
2. C.-C. Chen and J. Maier, Decoupling electron and ion storage and the path from interfacial storage to artificial electrodes, *Nat. Energy*, 2018, **3**, 102-108.
3. Q. Li, H. Li, Q. Xia, Z. Hu, Y. Zhu, S. Yan, C. Ge, Q. Zhang, X. Wang, X. Shang, S. Fan, Y. Long, L. Gu, G. X. Miao, G. Yu and J. S. Moodera, Extra storage capacity in transition metal oxide lithium-ion batteries revealed by in situ magnetometry, *Nat. Mater.*, 2021, **20**, 76-83.
4. S. Grugeon, S. Laruelle, L. Dupont and J. M. Tarascon, An update on the reactivity of nanoparticles Co-based compounds towards Li, *Solid State Sci.*, 2003, **5**, 895-904.
5. S. Laruelle, S. Grugeon, P. Poizot, M. Dollé, L. Dupont and J.-M. Tarascon, On the Origin of the Extra Electrochemical Capacity Displayed by MO/Li Cells at Low Potential, *J. Electrochem. Soc.*, 2002, **149**, A627-A634.
6. H. Li, Z. Hu, Q. Xia, H. Zhang, Z. Li, H. Wang, X. Li, F. Zuo, F. Zhang, X. Wang, W. Ye, Q. Li, Y. Long, Q. Li, S. Yan, X. Liu, X. Zhang, G. Yu and G. X. Miao, Operando Magnetometry Probing the Charge Storage Mechanism of CoO Lithium-Ion Batteries, *Adv. Mater.*, 2021, **33**, e2006629.
7. J. P. Perdew, K. Burke and M. Ernzerhof, Generalized Gradient Approximation Made Simple, *Phys. Rev. Lett.*, 1996, **77**, 3865.
8. G. Kresse and J. Furthmüller, Efficient iterative schemes for ab initio total-energy calculations using a plane-wave basis set, *Phys. Rev. B*, 1996, **54**, 11169.
9. G. Kresse and D. Joubert, From ultrasoft pseudopotentials to the projector augmented-wave method, *Phys. Rev. B*, 1999, **59**, 1758.
10. Y. Wang, P. Wisesa, A. Balasubramanian, S. Dwaraknath and T. Mueller, Rapid generation of optimal generalized Monkhorst-Pack grids, *Comput. Mater. Sci.*, 2021, **187**, 110100.
11. V. Wang, N. Xu, J.-C. Liu, G. Tang and W.-T. Geng, VASPKIT: A user-friendly interface facilitating high-throughput computing and analysis using VASP code, *Comput. Phys. Commun.*, 2021, **267**, 108033.